

# Neutron star cooling implications and magnetic field of the Vela Junior central compact object from all XMM-Newton and Chandra spectra

Wynn C. G. Ho,<sup>1</sup>★ Esther Simkhayeva,<sup>1</sup> and Alexander Y. Potekhin<sup>2</sup>

<sup>1</sup>Department of Physics and Astronomy, Haverford College, 370 Lancaster Avenue, Haverford, PA 19041, USA

<sup>2</sup>Ioffe Institute, Politekhnicheskaya 26, Saint Petersburg, 194021, Russia

Accepted 2026 January 16. Received 2026 January 13; in original form 2025 December 14

## ABSTRACT

The central compact object (CCO) in the Vela Junior supernova remnant is a young neutron star whose relatively low X-ray flux and small distance suggest it has a mass high enough to activate fast neutrino cooling processes. Here we analyse all XMM-Newton MOS and pn and Chandra ACIS-S spectra of the Vela Junior CCO, with observations taking place over the 9 years from 2001 to 2010. We find that the best-fit flux and spectral model parameters do not vary significantly when treating each observation independently, and therefore we fit all the spectra simultaneously using various spectral models to characterize the predominantly thermal emission from the neutron star surface. Our results indicate the Vela Junior CCO has an atmosphere composed of hydrogen, a hot spot temperature (unredshifted) of  $3.5 \times 10^6$  K, and a colder surface temperature of  $(6.6 - 8.8) \times 10^5$  K. Possible absorption lines at  $\approx 0.6$  keV and 0.9 keV provide evidence for the first-time of an average surface magnetic field  $B \approx 3 \times 10^{10}$  G for this CCO, which is similar to the magnetic field of other CCOs. At the accurate new Vela Junior distance of 1.4 kpc, the observed luminosity that is dominated by the hot spot is  $\sim 5 \times 10^{32}$  erg s<sup>-1</sup>. The luminosity from the rest of the colder surface is  $(1.3 - 4.0) \times 10^{32}$  erg s<sup>-1</sup>. The cool luminosity and temperature imply the Vela Junior CCO is indeed colder than many other young neutron stars and probably has a high mass that triggered fast neutrino cooling.

**Key words:** dense matter – stars: magnetic fields – stars: neutron – supernovae: individual: Vela Junior – X-rays: stars

## 1 INTRODUCTION

The cooling behaviour of neutron stars (NSs) is a crucial probe for uncovering properties of nuclear matter at high densities (see, e.g., Potekhin et al. 2015; Burgio et al. 2021, for review). For example, the rapid real-time cooling measured over more than two decades of the NS in the Cassiopeia A supernova remnant (SNR) can be explained by neutrino emission due to Cooper pair breaking and formation processes and thus provides constraints on the critical energy gaps/temperatures of nucleon superconductivity and superfluidity (Page et al. 2011; Shternin et al. 2011, 2023; Zhao et al. 2025). Alternatively, this rapid cooling can be explained by direct Urca processes, which are more efficient than pair breaking and formation but only predicted to occur for some nuclear equations of state (Lattimer et al. 1991; Page & Applegate 1992), and thus can constrain characteristics of the NS core (see, e.g., Potekhin & Yakovlev 2026). Another example is the low observed temperature of a small number of young NSs (see, e.g., Page et al. 2004), including the NS in the Vela Junior SNR (Potekhin et al. 2020; Marino et al. 2024), which also point to fast direct Urca cooling. Here we re-evaluate the Vela Junior NS in this context and in light of its recent distance determination (Suherli et al. 2026) and much more data simultaneously analysed together than done previously.

The Vela Junior SNR (also known as RX J0852.0–4622 and

G266.2–1.2) is young, with an age of 2.4–5.1 kyr (Allen et al. 2015), and hosts CXOU J085201.4–461753, a NS that was confirmed by Chandra (Pavlov et al. 2001) soon after discovery of the SNR (Aschenbach 1998). This NS is one member of a class of NSs known as central compact objects (CCOs). CCOs are made up of about a dozen young NSs that are located near the centre of their associated SNR and are nearly only seen to radiate constant thermal X-ray emission from their surface (De Luca 2008, 2017; Gotthelf et al. 2013).

CCOs also appear to possess low magnetic fields ( $\lesssim 10^{11}$  G) compared to most young pulsars and NSs, with the main evidence coming from the only three CCOs whose spin period  $P$  and time derivative of period  $\dot{P}$  have been measured. Attributing each CCO’s spin-down rate  $\dot{P}$  to energy loss by magnetic dipole radiation, PSR J0821–4300 with  $P = 112$  ms in the Puppis A SNR has a magnetic field  $B = 2.9 \times 10^{10}$  G (Gotthelf & Halpern 2009; Gotthelf et al. 2013), PSR J1210–5226 (also known as 1E 1207.4–5209) with  $P = 424$  ms has  $B = 9.8 \times 10^{10}$  G (Zavlin et al. 2000; Gotthelf et al. 2013), and PSR J1852+0040 with  $P = 105$  ms in the Kesteven 79 SNR has  $B = 3.1 \times 10^{10}$  G (Gotthelf et al. 2005; Halpern & Gotthelf 2010); note these values of  $B$  are the fields at the NS equator. For comparison, the spectrum of 1E 1207.4–5209 shows clear absorption lines at 0.7 and 1.4 keV that can be attributed to electron cyclotron resonance and its first harmonic at  $B = (7 - 8) \times 10^{10}$  G (Sanwal et al. 2002; Mereghetti et al. 2002; Bignami et al. 2003; Suleimanov et al. 2012), and the spectrum of PSR J0821–4300 appears to have a ro-

★ E-mail: who@haverford.edu

**Table 1.** Log of observations used in present work.

Instrument	ObsID	Observation Date	Exposure (ks)
Chandra ACIS-S	1034	2001 Sep 17	31
XMM-Newton MOS	0112870601	2001 Apr 27	25
XMM-Newton MOS+pn	0147750101	2003 May 21	56
XMM-Newton MOS+pn	0147750201	2003 Jun 25	17
XMM-Newton MOS+pn	0207300101	2005 Jun 2	54
XMM-Newton MOS+pn	0652510101	2010 Nov 13	85

tation phase-dependent feature(s) at 0.46 or 0.75 keV that implies  $B \sim 5 \times 10^{10}$  G if also interpreted as being due to electron cyclotron resonance (Gotthelf & Halpern 2009; Gotthelf et al. 2013).

After the Vela Junior CCO (hereafter, we refer for simplicity to the NS/CCO as Vela Junior) was confirmed and its position of  $R.A. = 08^{\text{h}}52^{\text{m}}01^{\text{s}}38$ ,  $\text{decl.} = -46^{\circ}17'53''34$  (J2000) was derived using a short 3 ks Chandra ACIS-I observation in 2000 (ObsID 1032; Pavlov et al. 2001), Vela Junior was observed twice more with Chandra. These two are a 31 ks observation in 2001 using ACIS-S in continuous clocking mode (ObsID 1034) and a 28 ks observation in 2009 using HRC-I (ObsID 10702). While the ACIS-S observation was used to study the spectrum of Vela Junior (Kargaltsev et al. 2002; Marino et al. 2024), the HRC-I observation was used along with the ACIS-I observation to derive a  $3\sigma$  upper limit of 300 mas  $\text{yr}^{-1}$  on the proper motion of Vela Junior (Mignani et al. 2019; see also Camilli et al. 2023). Meanwhile, XMM-Newton observed Vela Junior five times from 2001 to 2010, as listed in Table 1. Various works used different subsets of the XMM-Newton observations to study the spectrum of Vela Junior, fitting it with various single or multi-component models (Becker et al. 2006; Potekhin et al. 2020; Wu et al. 2021; Alford & Halpern 2023). A summary of the main spectral results from these previous analyses are given in Table 2.

In our present work, we analyse all the XMM-Newton data and the Chandra ACIS-S data together for the first time, and we conduct fits to the spectra systematically using different models. An outline of the paper is as follows. Section 2 describes the Chandra and XMM-Newton data analysed in this work and their processing. Section 3 presents our results. Section 4 summarizes our findings and discusses their implications for NS cooling and dense nuclear matter.

## 2 DATA ANALYSIS

### 2.1 Chandra data

Chandra observed Vela Junior using the ACIS-S detector in continuous clocking (CC) mode on 2001 September 17 (ObsID 1034) for 31 ks. Meanwhile, we ignore the short 3 ks ACIS-I observation from 2000 October 26 (ObsID 1032) and the poorer spectral resolution 28 ks HRC-I observation from 2009 November 13 (ObsID 10702). We reprocess the ACIS-S data following the standard procedure using `chandra_repro` of the Chandra Interactive Analysis of Observations (CIAO) package version 4.17 and Calibration Database (CALDB) 4.12.0 (Fruscione et al. 2006). We follow the recommended procedure for extracting source events from CC mode data<sup>1</sup>. Using `specextract`, source events are extracted from a rotated  $6 \times 4$  pixel box centred on the CCO position, while two rotated

$14 \times 4$  pixel boxes on either side are used for background. Spectra are binned using `dmgroup` with a minimum of 100 counts per bin.

### 2.2 XMM-Newton data

XMM-Newton EPIC observed Vela Junior on five occasions, as shown in Table 1. The first observation in 2001 (ObsID 0112870601) was pointed more than 2 arcmin off-axis from Vela Junior; furthermore, the source fell on a gap on the pn detector, and therefore we ignore this pn data. All MOS observations are in full frame mode, while pn observations are in small window mode. We process MOS and pn observation data files (ODFs) using the Science Analysis Software (SAS) 22.0.0 tasks `emproc` and `epproc`, respectively. To remove periods of background flaring, we extract single event (PATTERN = 0), high energy ( $> 10$  keV for MOS and  $10 - 12$  keV for pn) light curves from which we determine low and steady count rate thresholds of  $0.8 - 2.5$  counts  $\text{s}^{-1}$  for MOS and  $0.1 - 0.2$  counts  $\text{s}^{-1}$  for pn, depending on the observation. These thresholds are used to generate good time intervals (GTIs) with `tabgtigen`, and the GTIs are then used to produce flare-cleaned events with `evtselect`. The resulting data have effective exposure times for ObsID 0112870601 of 8 ks each for MOS1 and MOS2, for ObsID 0147750101 of 38 ks each for MOS1 and MOS2 and 28 ks for pn, for ObsID 0147750201 of 15 ks each for MOS1 and MOS2 and 11 ks for pn, for ObsID 0207300101 of 49 ks each for MOS1 and MOS2 and 36 ks for pn, for ObsID 0652510101 of 70 ks for MOS1, 69 ks for MOS2, and 51 ks for pn.

To extract MOS and pn source counts, we use circular regions with radii of 24 arcsec and 20 arcsec, respectively. To determine the background, we use annuli with inner and outer radii of 25 arcsec and 40 arcsec for MOS and 22 arcsec and 40 arcsec for pn. Using `epatplot`, we do not find the source counts to be significantly affected by pile-up. Source and background counts for spectral analysis are extracted using PATTERN  $\leq 12$  and  $\leq 4$  for MOS and pn, respectively, and FLAG = 0 for spectra. We calculate source and background areas and account for bad pixels and chip gaps using `backscale`. We then compute rmf and arf files. MOS1 and MOS2 spectra are combined using `epicspeccombine`. The two 2003 observations, ObsIDs 0147750101 and 0147750101, are also combined since they took place only about one month apart. Spectra are binned using `specgroup` to a minimum of 100 counts per bin for the combined MOS spectrum and for the pn spectrum.

### 2.3 Spectral modelling

We perform spectral fitting using Xspec 12.15.0 (Arnaud 1996) and consider the energy range 0.5–8 keV. The spectral models used here are composed of several components. When fitting across instruments, we include the constant model, in order to account for instrumental differences between ACIS-S, MOS, and pn spectral normalizations, and we fix its value to 1 for pn spectra and allow it to vary for the ACIS-S spectrum and the combined MOS spectra. Next, we include a component to account for photoelectric absorption by the interstellar medium, i.e. `tbabs` with abundances from Wilms et al. (2000) and cross-sections from Verner et al. (1996) and parametrized by the effective hydrogen column density  $N_{\text{H}}$ .

The final component(s) used, which models the intrinsic spectrum of Vela Junior, is either a blackbody (BB; `bbbodyrad`), a NS atmosphere, or a power law (PL; `powerlaw`). The blackbody is parametrized by the redshifted temperature  $kT^{\infty}$  and normalization  $R^{\infty}/d$ , where  $T^{\infty} = T/(1 + z_g)$ ,  $R^{\infty} = R(1 + z_g)$ , distance is  $d$ , redshift factor is  $1 + z_g = 1/(1 - 2GM/c^2R)^{1/2}$ , and NS mass is

<sup>1</sup> [https://cxc.cfa.harvard.edu/ciao/caveats/acis\\_cc\\_mode.html](https://cxc.cfa.harvard.edu/ciao/caveats/acis_cc_mode.html)

**Table 2.** Spectral modelling results from previous works using blackbody (BB), neutron star atmosphere (carbatm, hatm, nsa, nsmaxg, nsx), and/or power law (PL) models. Here,  $kT$  (and  $kT_2$ ) refers to  $kT^\infty$  for a blackbody model or  $kT_{\text{eff}}$  for an atmosphere model and similarly for the radius  $R$ , relative to distance  $d$ . Errors are  $1\sigma$ , except for those from Potekhin et al. (2020); Marino et al. (2024) which are at 90 percent confidence and those from Alford & Halpern (2023) which are at unknown confidence. See text for more details.

Reference work	Dataset	Spectral model	$N_{\text{H}}$ ( $10^{21} \text{ cm}^{-2}$ )	$kT$ (eV)	$R/d$ (km/kpc)	$kT_2$ or $\Gamma$ (eV)	$R_2/d$ (km/kpc)	$\chi^2/\text{dof}$
Kargaltsev et al. 2002	ACIS-S	BB	$3.45 \pm 0.15$	$404 \pm 5$	$0.28 \pm 0.01$	$< 89$	10	84/74
Kargaltsev et al. 2002	ACIS-S	nsa		270	1.2			
Becker et al. 2006	MOS+pn 2001+2003	BB	$3.22^{+0.14}_{-0.13}$	$391 \pm 4$	$0.285^{+0.009}_{-0.008}$			521/431
Becker et al. 2006	MOS+pn 2001+2003	BB+BB	$3.82^{+0.36}_{-0.30}$	$343^{+24}_{-40}$	$0.36^{+0.05}_{-0.03}$	$569^{+261}_{-101}$	$0.059^{+0.064}_{-0.043}$	465/429
Becker et al. 2006	MOS+pn 2001+2003	BB+PL	$7.63^{+0.72}_{-1.59}$	$366^{+10}_{-13}$	$0.30^{+0.03}_{-0.02}$	$4.21^{+0.30}_{-0.59}$		469/429
Potekhin et al. 2020 <sup>a</sup>	MOS+pn 2003–2010	nsx [carbon]	$6.8 \pm 0.1$	$133 \pm 2$	$5.0 \pm 0.4$			920/913
Wu et al. 2021	pn 2010	BB+BB	$5.5^{+0.6}_{-0.5}$	$317^{+33}_{-44}$	$0.39^{+0.08}_{-0.04}$	$482^{+89}_{-43}$	$0.12^{+0.07}_{-0.06}$	59/68
Wu et al. 2021	pn 2010	hatm+hatm	$7.96^{+0.67}_{-1.10}$	$256^{+6}_{-5}$	0.95	$71^{+5}_{-9}$	12	61/69
Wu et al. 2021	pn 2010	carbatm	$7.0 \pm 0.2$	$145 \pm 3$	4.3			60/70
Alford & Halpern 2023	pn 2005	carbatm	$4.70 \pm 0.12$	$132 \pm 0.4$	5.2			82/73
Alford & Halpern 2023	pn 2010	carbatm	$4.91 \pm 0.11$	$132 \pm 0.3$	5.2			87/80
Marino et al. 2024	ACIS-S	BB	$4.7 \pm 0.4$	$397 \pm 9$	$0.24 \pm 0.08$	$< 50$	11	162/143
Marino et al. 2024	ACIS-S	nsmaxg [ $10^{12} \text{ G}$ ]		$310 \pm 10$	$0.50^{+0.07}_{-0.05}$			

<sup>a</sup> P. Shternin, private comm.

$M$  and radius is  $R$ . The NS atmosphere models we use (nsx and nsmaxg; see below) have similar parameters, in particular, effective temperature  $kT_{\text{eff}}$ ,  $M$ ,  $R$ ,  $d$ , and normalization  $R_{\text{em}}/R$ , where  $R_{\text{em}}$  is emission region radius, as well as atmosphere composition and, in the case of nsmaxg, magnetic field strength  $B$ . Previous works showed that a single power law is a poor fit to Vela Junior spectra (Kargaltsev et al. 2002; Becker et al. 2006), and we also find this to be the case. However, we do consider models where a power law is used in combination with a blackbody or atmosphere. The power law is parametrized by photon index  $\Gamma$  and normalization. In summary, we model the intrinsic Vela Junior spectrum by either a single component made up of a blackbody or atmosphere spectrum that represents a hot spot on the NS surface or two components made up of two blackbodies (BB+BB) or two atmospheres, a blackbody and a power law (BB+PL), or an atmosphere and a power law. For the two (temperature) atmospheres case, the second (cooler) atmosphere has a fixed normalization  $R_{\text{em}}/R = 1$  to represent emission from the rest of the NS surface besides the hot spot. Once a best-fit is found, we use cflux to calculate flux and its uncertainties while holding all other model parameters at their best-fit values.

For NS atmosphere models, we consider two types of models, depending on the unknown surface magnetic field of Vela Junior. The first are those computed for partially ionized hydrogen or carbon in the low/non-magnetic regime when  $B \lesssim 10^9 \text{ G}$  (nsx; Ho & Heinke 2009). A non-magnetic helium atmosphere (via nsx) yields fits that are comparable to those of hydrogen and carbon and give model parameter values in between those of hydrogen and carbon. However, a helium or carbon atmosphere is unlikely to be present for isolated NSs at the age and temperature of Vela Junior (Chang et al. 2010; Wijngaarden et al. 2019), and thus we do not show our helium results. On the other hand, we show our carbon results so that they can be compared to results from previous works (see Table 2). The second type of models are those for partially ionized hydrogen at a single

$B$  in the range  $10^{10} \text{ G} \leq B \leq 3 \times 10^{13} \text{ G}$  (nsmaxg<sup>2</sup>; Ho et al. 2008; Ho 2014; Potekhin et al. 2014). We note that the four atmosphere models with varying magnetic fields and surface temperatures in nsmaxg do not fit the data well when used as the only component for the intrinsic Vela Junior spectrum, but they can fit the data when used in combination with a power law. Meanwhile, partially ionized carbon, oxygen, and neon atmosphere models at  $10^{12} \text{ G}$  and  $10^{13} \text{ G}$  (via nsmaxg; Mori & Ho 2007) also do not fit the data, so will not be discussed further. For all atmosphere spectral fits, model parameters for NS mass and radius are fixed to  $M = 1.4 M_{\odot}$  and  $R = 12 \text{ km}$ , respectively; as a consequence, a factor  $1 + z_g = 1.235$  is used to convert between redshifted and unredshifted values when needed. We note that a small change in the fixed mass, e.g., to  $1.6 M_{\odot}$ , and hence redshift factor, leads to small differences in best-fit values that are mostly within the uncertainties.

### 3 RESULTS

We start by fitting each dataset with a single component absorbed blackbody. Our best-fit results are given in Table 3. Individually, some of the datasets can be fit well with a blackbody, while others are not well-fit, and they all indicate emission primarily from a small ( $R^\infty \sim 0.3 \text{ km}$  at 1 kpc) hot spot on the NS surface. The quality of the fit depends in large part on whether the spectra at  $\gtrsim 3 \text{ keV}$  are taken into account. For example, the MOS spectrum from 2001 (from a 8 ks effective exposure taken off-axis; see Section 2.2) spans only 0.7–3 keV with our binning. Even though the flux at  $> 3 \text{ keV}$  is low, a single blackbody at  $kT^\infty \approx 400 \text{ eV}$  fails to characterize this high-energy emission, as noted by Becker et al. (2006). We find a very similar temperature and radius when comparing our results to previous works that fit single blackbodies to specific datasets, while our best-fit  $N_{\text{H}} \sim 4.3 \times 10^{21} \text{ cm}^{-2}$  is somewhat different from

<sup>2</sup> <https://heasarc.gsfc.nasa.gov/docs/software/xspec/manual/node208.htm>

**Table 3.** Spectral modelling results using bbodyrad (BB), where all parameters are free to vary between datasets. Absorbed 0.5–8 keV flux  $f_{0.5-8}^{\text{abs}}$  is in units of  $10^{-12} \text{ erg cm}^{-2} \text{ s}^{-1}$ . Errors are  $1\sigma$ . For the simultaneous fit of all datasets shown in the last row, two additional parameters are included in the fit: a constant MOS/pn normalization and a constant ACIS-S/pn normalization; the best-fit for these two are  $0.969 \pm 0.006$  and  $1.12 \pm 0.01$ , respectively.

Dataset	$N_{\text{H}}$ ( $10^{21} \text{ cm}^{-2}$ )	$kT^{\infty}$ (eV)	$R^{\infty}/d$ (m/kpc)	$f_{0.5-8}^{\text{abs}}$	$\chi^2/\text{dof}$
ACIS-S	$4.13^{+0.21}_{-0.20}$	$404^{+5}_{-5}$	$278^{+9}_{-9}$	$1.42 \pm 0.01$	86/73
MOS 2001	$4.08^{+0.59}_{-0.56}$	$397^{+15}_{-14}$	$269^{+29}_{-23}$	$1.24 \pm 0.03$	22/22
MOS 2003	$4.31^{+0.20}_{-0.19}$	$393^{+4}_{-4}$	$277^{+8}_{-7}$	$1.22 \pm 0.01$	84/61
MOS 2005	$4.30^{+0.22}_{-0.22}$	$400^{+4}_{-4}$	$264^{+8}_{-8}$	$1.21 \pm 0.01$	60/57
MOS 2010	$4.30^{+0.17}_{-0.17}$	$395^{+3}_{-3}$	$273^{+7}_{-6}$	$1.217 \pm 0.009$	87/66
pn 2003	$4.29^{+0.16}_{-0.15}$	$396^{+4}_{-4}$	$271^{+7}_{-7}$	$1.23 \pm 0.01$	71/62
pn 2005	$4.07^{+0.17}_{-0.16}$	$396^{+4}_{-4}$	$275^{+8}_{-7}$	$1.27 \pm 0.01$	74/54
pn 2010	$4.40^{+0.14}_{-0.14}$	$395^{+3}_{-3}$	$278^{+6}_{-6}$	$1.259 \pm 0.009$	62/59
all	$4.27^{+0.07}_{-0.06}$	$396^{+1}_{-1}$	$275^{+3}_{-3}$	$1.246 \pm 0.004$	573/472

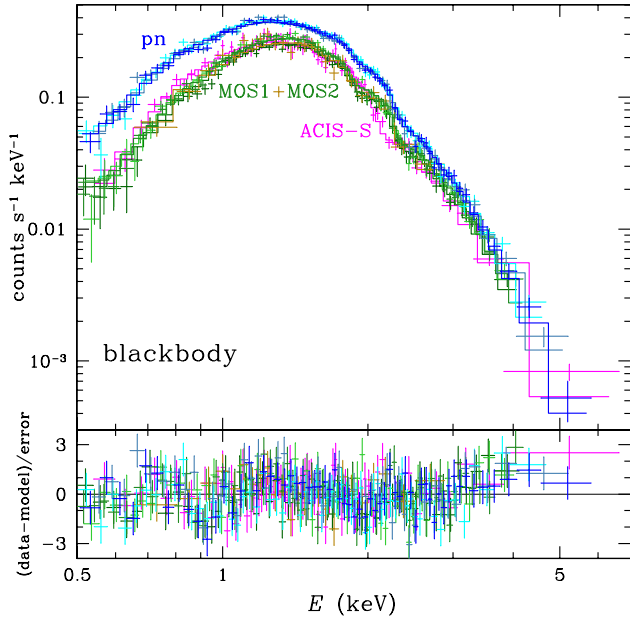


**Figure 1.** Spectra of Vela Junior from Chandra ACIS-S and XMM-Newton MOS1+MOS2 and pn data. Top panel shows data with  $1\sigma$  errors (crosses) and spectral model made up of a single blackbody. Bottom panel shows  $\chi^2 = (\text{data}-\text{model})/\text{error}$ .

the results of Kargaltsev et al. (2002); Becker et al. (2006) but is consistent with that of Marino et al. (2024) (see Table 2). Finally, from Table 3 and as we shall show below, the spectra do not appear to vary significantly from 2001 to 2010, and therefore we fit all the datasets together with one absorbed blackbody. The results are given in Table 3 and shown in Figure 1. We see the fit quality is not good ( $\chi^2/\text{dof} = 573/472 = 1.21$ ), and the model fit residual shows wave-like systematics and underprediction of the data at  $> 3$  keV.

To better characterize the spectra of Vela Junior, we fit each dataset using a multi-component absorbed double blackbody (BB+BB) or blackbody plus power law (BB+PL). The best-fit results are shown

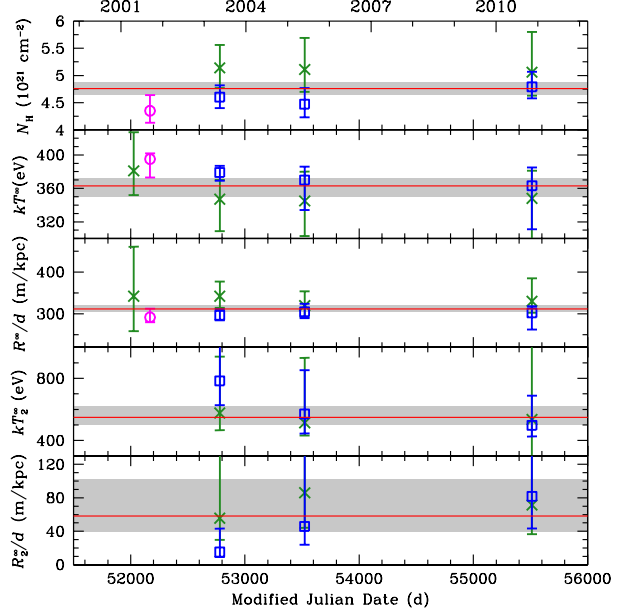


**Figure 2.** Interstellar absorption  $N_{\text{H}}$  and blackbody temperatures  $kT^{\infty}$  and  $kT_2^{\infty}$  and emission radii  $R^{\infty}$  and  $R_2^{\infty}$  (relative to distance  $d$ ) for a bbodyrad+bbodyrad (BB+BB) model fit to ACIS-S (circles), MOS (crosses), and pn (squares) spectra. Errors are  $1\sigma$ . Some values for the ACIS-S and MOS 2001 fits are not shown because they lie outside displayed ranges due to these data being of lower quality (see text for details). Horizontal solid lines show results for a simultaneous fit to all the data, and the shaded regions encompass the  $1\sigma$  error.

in Tables 4 and 5 and Figures 2 and 3. First, note that the addition of a second component, whether a blackbody or power law, does not significantly improve the goodness-of-fit of the ACIS-S spectrum, and thus this extra component is not particularly justified by the data. In fact, such a conclusion is evident by the best-fit parameters of the additional component which has a poorly constrained temperature and small emission radius for the second blackbody and a low normalization for the power law and hence a very small contribution to the spectrum. Also of note in the best-fit to the MOS 2001 spectrum is its poorly constrained and unrealistic parameter values for the extra component and  $N_{\text{H}}$ , which is due to the spectrum's limited energy range, as noted above. Comparing the remaining results to those from the single blackbody fits, the addition of a second component leads to a decrease of 20–50 eV in the blackbody temperature and a small increase of the emission radius (of the cooler blackbody). In addition, for the double blackbody fits, one can see that the temperature (emission radius) of the cooler blackbody for the MOS spectra are consistently lower (higher), but within the uncertainties, than those for the pn spectra; this is likely due to the lower sensitivity, and hence flux normalization, of MOS compared to pn. Our results are also generally consistent with those from previous works (see Table 2, in particular, Becker et al. 2006; Wu et al. 2021). We note that if one of the two blackbody radii is fixed to  $\sim 12$  km, which is much larger than either best-fit emission radii when they are both allowed to vary (see Table 4), then the corresponding temperature is so low that this blackbody component does not contribute significantly to the best-fit model and the results are essentially the same as those of a single blackbody model (see Table 3).

It is again evident that the best-fit model parameters do not differ significantly between the individual observations from 2001 to

**Table 4.** Spectral modelling results using `bbodyrad+bbodyrad` (BB+BB), where all parameters are free to vary between datasets. Absorbed 0.5–8 keV flux  $f_{0.5-8}^{\text{abs}}$  is in units of  $10^{-12}$  erg cm $^{-2}$  s $^{-1}$ . Errors are  $1\sigma$ . For the simultaneous fit of all datasets shown in the last row, two additional parameters are included in the fit: a constant MOS/pn normalization and a constant ACIS-S/pn normalization; the best-fit for these two are  $0.968 \pm 0.006$  and  $1.12 \pm 0.01$ , respectively.

Dataset	$N_{\text{H}}$ ( $10^{21}$ cm $^{-2}$ )	$kT^{\infty}$ (eV)	$R^{\infty}/d$ (m/kpc)	$kT_2^{\infty}$ (eV)	$R_2^{\infty}/d$ (m/kpc)	$f_{0.5-8}^{\text{abs}}$	$\chi^2/\text{dof}$
ACIS-S	$4.35^{+0.29}_{-0.22}$	$395^{+7}_{-22}$	$292^{+21}_{-12}$	$1700^{+0}_{-1200}$	$3^{+60}_{-3}$	$1.44 \pm 0.01$	82/72
MOS 2001	$13.9^{+3.5}_{-4.2}$	$381^{+46}_{-29}$	$342^{+118}_{-83}$	$127^{+41}_{-19}$	$8600^{+13000}_{-3000}$	$1.24 \pm 0.03$	15/20
MOS 2003	$5.14^{+0.42}_{-0.37}$	$347^{+23}_{-38}$	$342^{+35}_{-28}$	$577^{+363}_{-111}$	$56^{+89}_{-26}$	$1.23 \pm 0.01$	67/59
MOS 2005	$5.11^{+0.58}_{-0.41}$	$345^{+35}_{-42}$	$319^{+34}_{-27}$	$514^{+418}_{-82}$	$86^{+180}_{-42}$	$1.21 \pm 0.01$	50/55
MOS 2010	$5.06^{+0.74}_{-0.43}$	$348^{+33}_{-88}$	$330^{+55}_{-27}$	$535^{+1600}_{-274}$	$71^{+270}_{-35}$	$1.225 \pm 0.009$	70/64
pn 2003	$4.60^{+0.22}_{-0.20}$	$379^{+8}_{-10}$	$296^{+15}_{-12}$	$783^{+246}_{-156}$	$15^{+28}_{-6}$	$1.24 \pm 0.01$	61/60
pn 2005	$4.47^{+0.30}_{-0.24}$	$370^{+16}_{-36}$	$305^{+20}_{-15}$	$571^{+282}_{-126}$	$46^{+156}_{-22}$	$1.28 \pm 0.01$	66/52
pn 2010	$4.79^{+0.28}_{-0.21}$	$363^{+22}_{-52}$	$302^{+16}_{-40}$	$497^{+192}_{-71}$	$82^{+200}_{-38}$	$1.264 \pm 0.009$	55/57
all	$4.76^{+0.12}_{-0.11}$	$363^{+9}_{-13}$	$311^{+8}_{-7}$	$548^{+71}_{-50}$	$58^{+44}_{-19}$	$1.254 \pm 0.004$	508/470

**Table 5.** Spectral modelling results using `bbodyrad+powerlaw` (BB+PL), where all parameters are free to vary between datasets. Absorbed 0.5–8 keV flux  $f_{0.5-8}^{\text{abs}}$  is in units of  $10^{-12}$  erg cm $^{-2}$  s $^{-1}$ . Errors are  $1\sigma$ . For the simultaneous fit of all datasets shown in the last row, two additional parameters are included in the fit: a constant MOS/pn normalization and a constant ACIS-S/pn normalization; the best-fit for these two are  $0.969 \pm 0.006$  and  $1.12 \pm 0.01$ , respectively.

Dataset	$N_{\text{H}}$ ( $10^{21}$ cm $^{-2}$ )	$kT^{\infty}$ (eV)	$R^{\infty}/d$ (m/kpc)	$\Gamma$	PL norm ( $10^{-4}$ cm $^{-2}$ s $^{-1}$ keV $^{-1}$ )	$f_{0.5-8}^{\text{abs}}$	$\chi^2/\text{dof}$
ACIS-S	$4.4^{+4.6}_{-0.3}$	$394^{+7}_{-19}$	$292^{+23}_{-7}$	$1.4^{+3.7}_{-1.4}$	$0.1^{+9.3}_{-0.1}$	$1.44 \pm 0.02$	82/72
MOS 2001	$18.0^{+4.4}_{-4.7}$	$393^{+25}_{-24}$	$305^{+120}_{-74}$	$7.1^{+1.5}_{-1.7}$	$70^{+97}_{-49}$	$1.24 \pm 0.03$	16/22
MOS 2003	$8.0^{+1.7}_{-3.3}$	$362^{+9}_{-8}$	$306^{+21}_{-22}$	$3.5^{+0.5}_{-2.6}$	$6.3^{+5.0}_{-6.1}$	$1.26 \pm 0.01$	68/59
MOS 2005	$9.3^{+1.2}_{-2.2}$	$377^{+10}_{-9}$	$277^{+20}_{-18}$	$3.94^{+0.52}_{-0.65}$	$9.2^{+5.5}_{-5.2}$	$1.23 \pm 0.01$	48/55
MOS 2010	$10.0^{+1.2}_{-1.3}$	$375^{+9}_{-8}$	$280^{+17}_{-15}$	$4.15^{+0.38}_{-0.39}$	$12^{+4}_{-4}$	$1.239 \pm 0.009$	66/64
pn 2003	$9.0^{+0.9}_{-1.0}$	$378^{+5}_{-5}$	$291^{+10}_{-10}$	$4.19^{+0.26}_{-0.27}$	$8.3^{+2.6}_{-2.5}$	$1.24 \pm 0.01$	56/60
pn 2005	$7.2^{+1.3}_{-1.5}$	$377^{+5}_{-5}$	$301^{+9}_{-8}$	$3.80^{+0.38}_{-0.48}$	$4.5^{+2.9}_{-2.5}$	$1.29 \pm 0.01$	63/52
pn 2010	$8.0^{+1.3}_{-2.2}$	$377^{+4}_{-4}$	$305^{+8}_{-7}$	$4.05^{+0.37}_{-0.67}$	$5.4^{+3.3}_{-3.8}$	$1.269 \pm 0.009$	54/57
all	$8.6^{+0.5}_{-0.6}$	$377^{+2}_{-2}$	$295^{+4}_{-4}$	$4.02^{+0.15}_{-0.16}$	$7.6^{+1.4}_{-1.4}$	$1.263 \pm 0.004$	502/470

2010, except in some cases for the ACIS-S and MOS data from 2001 due to the former being taken in CC mode (and thus is partly contaminated by SNR emission due to data collection being collapsed in one spatial dimension) and the off-axis short exposure of the latter. Therefore we fit all the datasets together with either an absorbed double blackbody or an absorbed blackbody plus power law, with the best-fit results also shown in Tables 4 and 5 and Figures 2 and 3. We see that both multi-component spectral models provide decent fits to the data and are much better fits than the single blackbody model. Both multi-component model fits are comparable, with  $\chi^2/\text{dof} = 508/470 = 1.08$  for the BB+BB model being slightly worse than the  $\chi^2/\text{dof} = 502/470 = 1.07$  for the BB+PL model. The absorption  $N_{\text{H}} = 8.6^{+0.5}_{-0.6} \times 10^{21}$  cm $^{-2}$  for BB+PL [see also the BB+PL model of Becker et al. (2006) in Table 2] is higher than for purely thermal models and is on the upper end of the values  $(1-9) \times 10^{21}$  cm $^{-2}$  determined for the rims of the SNR but is still below the  $11 \times 10^{21}$  cm $^{-2}$  determined for diffuse emission in the SNR central region by Slane et al. (2001); Acero et al. (2013); Camilli et al. (2023). Also while the power law index  $\Gamma = 4$  is somewhat high, Becker et al. (2006) argued that these results by themselves do not mean the blackbody plus power law can be rejected.

We can disfavor the blackbody plus power law model however by examining more closely the contribution of the power law to modelling the spectra. A power law model is often used to characterize non-thermal emission at  $> 1$  keV from, e.g., a pulsar wind nebula. Figure 4 shows the simultaneous fit to all the spectra using a model composed of a NS atmosphere and power law (nsx+PL), which will be described in more detail below. In particular, the top panel displays the individual contributions of the atmosphere component and the power law component to mimicking the actual data. Our blackbody plus power law (BB+PL) spectral fits show very similar behaviour. What is particularly worth highlighting is that the power law component, while providing some significant flux at  $E \gtrsim 3$  keV, is the dominant spectral component at energies below 1 keV. This also explains the high inferred absorption  $N_{\text{H}}$  for the fits that include a power law since a higher absorption is needed to reduce the flux from the power law component at these low energies. This all suggests that here the power law is primarily acting as a substitute for a soft thermal component and is probably not a realistic description of the true spectrum of Vela Junior. Nevertheless, there still could be a non-thermal power law component at higher X-ray energies but at a much lower flux level than can be determined by the data.

Next, we fit all the spectra simultaneously using NS atmosphere

**Table 6.** Spectral modelling results using neutron star atmosphere models `nsx` and `nsmaxg` (hydrogen, unless otherwise noted). Model parameters that are held fixed are NS mass  $M = 1.4 M_{\odot}$  and radius  $R = 12$  km,  $R_{\text{em},2}/R = 1$ , and distance  $d = 1.4$  kpc, unless otherwise noted. Absorbed 0.5–8 keV flux  $f_{0.5-8}^{\text{abs}}$  is in units of  $10^{-12}$  erg cm $^{-2}$  s $^{-1}$ , and power law normalization is in units of  $10^{-4}$  cm $^{-2}$  s $^{-1}$  keV $^{-1}$ . Errors are  $1\sigma$ . A constant MOS/pn normalization and a constant ACIS-S/pn normalization is included in all fits; the best-fit for these two are  $0.967 \pm 0.006$  and  $1.12 \pm 0.01$ , respectively. For models with `gabs` components, Table 7 gives the best-fit values for the `gabs` parameters.

Model	$B$ ( $10^{11}$ G)	$N_{\text{H}}$ ( $10^{21}$ cm $^{-2}$ )	$kT_{\text{eff}}$ (eV)	$R_{\text{em}}$ (m)	$kT_{\text{eff},2}$ (eV)	$f_{0.5-8}^{\text{abs}}$	$\chi^2/\text{dof}$
<code>nsx</code> [carbon]	0	$6.81^{+0.06}_{-0.06}$	$149^{+1}_{-1}$	$5190^{+150}_{-140}$			$1.254 \pm 0.004$
<code>nsx</code>	0	$5.03^{+0.07}_{-0.06}$	$301^{+2}_{-2}$	$871^{+13}_{-10}$			$1.251 \pm 0.004$
<code>nsmaxg</code>	7	$4.75^{+0.09}_{-0.07}$	$307^{+2}_{-3}$	$824^{+18}_{-12}$			$1.246 \pm 0.004$
<code>nsx+nsx</code>	0	$5.68^{+0.47}_{-0.38}$	$298^{+2}_{-2}$	$897^{+17}_{-14}$	$57^{+7}_{-9}$		$1.251 \pm 0.004$
$(\text{nsx+nsx}) \times \text{gabs}$	0	$6.70^{+0.23}_{-0.29}$	$303^{+2}_{-3}$	$862^{+23}_{-19}$	$76^{+3}_{-4}$		$1.252 \pm 0.004$
$(\text{nsx+nsx}) \times \text{gabs} \times \text{gabs}$	0	$6.15^{+0.35}_{-0.50}$	$303^{+2}_{-3}$	$859^{+22}_{-18}$	$72^{+4}_{-6}$		$1.252 \pm 0.004$
<code>nsmaxg+nsmaxg</code>	$7+0.316$	$5.66^{+0.26}_{-0.29}$	$303^{+2}_{-3}$	$860^{+18}_{-12}$	$60^{+3}_{-5}$		$1.246 \pm 0.004$
<code>nsx+nsx</code> [ $d = 1$ kpc]	0	$5.67^{+0.66}_{-0.35}$	$298^{+2}_{-3}$	$645^{+17}_{-12}$	$50^{+8}_{-7}$		$1.251 \pm 0.004$
<code>nsmaxg+nsmaxg</code> [ $d = 1$ kpc]	$7+0.316$	$5.62^{+0.30}_{-0.29}$	$302^{+2}_{-3}$	$622^{+14}_{-12}$	$52^{+3}_{-4}$		$1.246 \pm 0.004$
$\Gamma$ PL norm							
<code>nsx+PL</code>	0	$8.42^{+0.64}_{-0.72}$	$287^{+2}_{-2}$	$967^{+17}_{-14}$	$4.33^{+0.22}_{-0.23}$	$5.6^{+1.6}_{-1.6}$	$1.257 \pm 0.004$
<code>nsmaxg+PL</code>	7	$8.41^{+0.62}_{-0.73}$	$285^{+2}_{-2}$	$957^{+19}_{-17}$	$4.19^{+0.21}_{-0.23}$	$6.1^{+1.6}_{-1.6}$	$1.257 \pm 0.004$

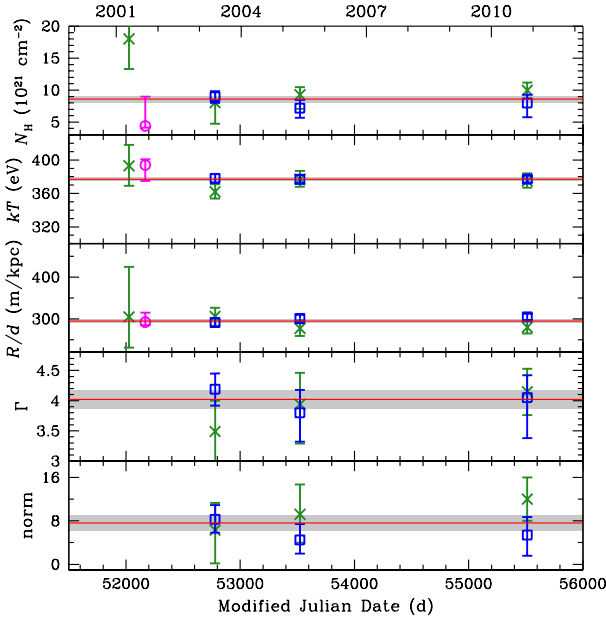


**Figure 3.** Interstellar absorption  $N_{\text{H}}$ , blackbody temperature  $kT^{\infty}$  and emission radius  $R^{\infty}$  (relative to distance  $d$ ), and power law index and normalization for a `bbodyrad+powerlaw` (BB+PL) model fit to ACIS-S (circles), MOS (crosses), and pn (squares) spectra. Errors are  $1\sigma$ . Some values for the ACIS-S and MOS 2001 fits are not shown because they lie outside displayed ranges due to these data being of lower quality (see text for details). Horizontal solid lines show results for a simultaneous fit to all the data, and the shaded regions encompass the  $1\sigma$  error.

models, i.e., non-magnetic `nsx` and magnetic `nsmaxg` (see Section 2.3). The best-fit results are given in Table 6. For a single component absorbed atmosphere model, a partially ionized non-

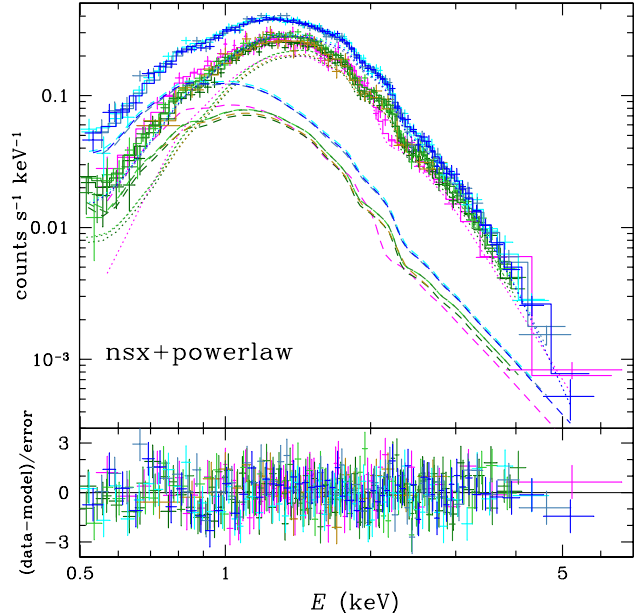


**Figure 4.** Spectra of Vela Junior from Chandra ACIS-S and XMM-Newton MOS1+MOS2 and pn data. Top panel shows data with  $1\sigma$  errors (crosses) and spectral model (`nsx+PL`) made up of a partially ionized non-magnetic hydrogen atmosphere component (dotted lines) and a power law component (dashed lines). Bottom panel shows  $\chi^2 = (\text{data}-\text{model})/\text{error}$ .

magnetic hydrogen atmosphere provides a satisfactory fit to the data, with  $\chi^2/\text{dof} = 515/472 = 1.09$ , and is almost as good as a model using two blackbodies. Non-magnetic carbon is not as good a fit as hydrogen but better than a single blackbody. Keeping in mind the relatively poorer fit we find for a carbon atmosphere, as well as the fit qualities found previously (see Table 2, in particular, Potekhin et al.

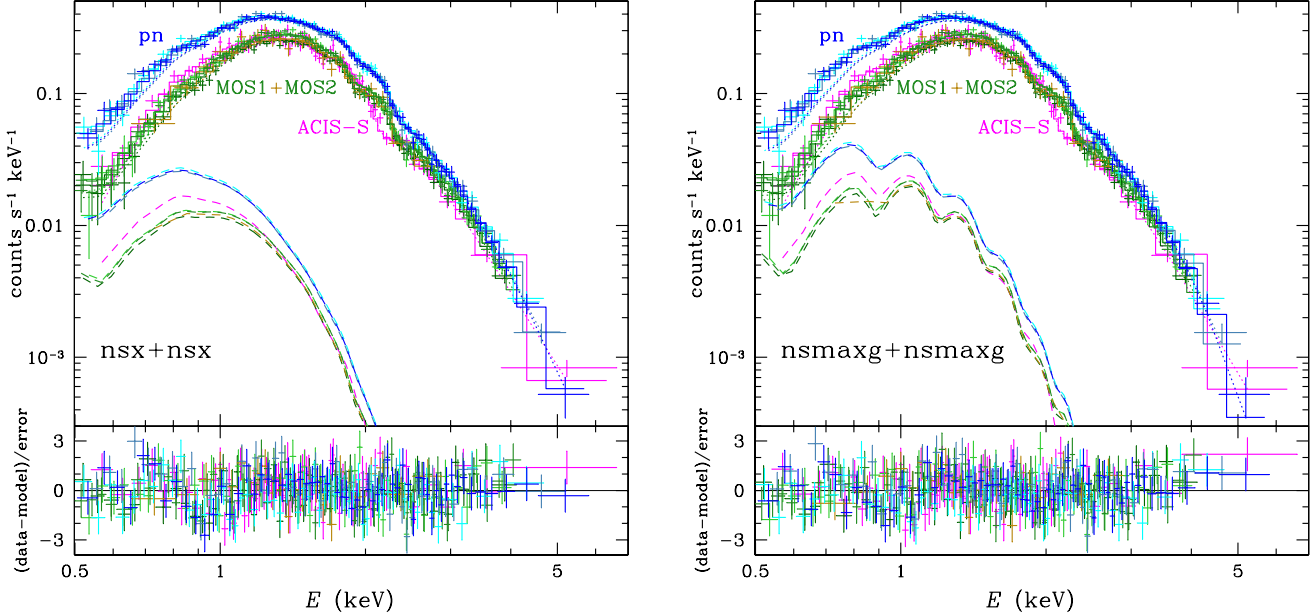


**Figure 5.** Spectra of Vela Junior from Chandra ACIS-S and XMM-Newton MOS1+MOS2 and pn data. Top panels show data with  $1\sigma$  errors (crosses) and spectral model made up of two partially ionized non-magnetic (nsx+nsx; left) and magnetic (nsmaxg+nsmaxg; right) hydrogen atmosphere components (dashed and dotted lines for cool and hot components, respectively). For the models on the right, the magnetic fields are  $B = 3.16 \times 10^{10}$  G and  $7 \times 10^{11}$  G for the cool and hot components, respectively. Bottom panels show  $\chi^2 = (\text{data}-\text{model})/\text{error}$ .

2020; Wu et al. 2021; Alford & Halpern 2023), our results are in broad agreement with those from previous works, except for a somewhat smaller  $R_{\text{em}}$  ( $= 3.7$  km) when scaled to 1 kpc and a higher temperature in some comparisons. For a magnetic hydrogen atmosphere, the two nsmaxg models at  $B = 7 \times 10^{11}$  G and  $9 \times 10^{11}$  G provide about the same quality of fits ( $\Delta\chi^2 = 2$ ) and parameters that are within their errors, except for a  $\sim 10$  percent difference in emitting radii. Poorer fits are obtained at  $B \leq 5 \times 10^{11}$  G, with  $\Delta\chi^2 \geq 92$ , and at  $B \geq 10^{12}$  G, with  $\Delta\chi^2 \geq 10$ .

Table 6 also gives results for fits using an absorbed atmosphere and power law model. We see that such models, with  $\Gamma > 4$ , can fit the data better than purely thermal models. However, as we pointed out above, the dominance of the power law component at low energies, as illustrated in Figure 4, and ensuing higher  $N_{\text{H}}$  argues against these models.

We perform two component absorbed atmosphere fits using the same sets of models as above. In this case though, we force the second component to have a fractional area  $R_{\text{em},2}/R = 1$ , so that this component represents emission from the whole star at an average temperature of  $T_{\text{eff},2}$ , while the first component is due to a small hot spot. The fit using non-magnetic hydrogen, with  $\chi^2/\text{dof} = 511/471 = 1.08$ , is a small improvement over the single component atmosphere fits and are as good as the double blackbody fit. Our results are broadly in agreement with those of Wu et al. (2021) (see also Table 2). Meanwhile, magnetic hydrogen with a small hot spot at  $B = 7 \times 10^{11}$  G and the remaining cool surface at  $B = 3.16 \times 10^{10}$  G and  $T_{\text{eff}} = 6.9 \times 10^5$  K gives a better fit, with  $\chi^2/\text{dof} = 503/471 = 1.07$ , than all the other purely thermal models tried so far. Figure 5 shows the partially ionized non-magnetic hydrogen atmosphere model (nsx+nsx) and magnetic hydrogen (nsmaxg+nsmaxg) results. We note for comparison that, if the second (colder) component has a magnetic field  $B = 5 \times 10^{11}$  G, the best-fit is worse by  $\Delta\chi^2 = 8$  and has a somewhat higher  $N_{\text{H}}$  and  $T_{\text{eff}}$ .

**Table 7.** Absorption line parameters from using non-magnetic hydrogen atmosphere models nsx+nsx and one or two Gaussian absorption line components gabs. Model parameters that are fixed are the same as given in Table 6, and other best-fit parameters are given there too. Errors are  $1\sigma$ .

	One line	Two lines
$E_1$ (eV)	$947^{+18}_{-20}$	$920^{+22}_{-25}$
width $\sigma_1$ (eV)	$122^{+27}_{-24}$	$133^{+28}_{-26}$
depth $d_1$ (eV)	$41^{+15}_{-11}$	$55^{+22}_{-19}$
$E_2$ (eV)		$635^{+14}_{-73}$
$\sigma_2$ (eV)		$5^{+82}_{-3}$
$d_2$ (eV)		$< 101$

While the distance to Vela Junior was recently pinpointed to  $1.41 \pm 0.14$  kpc (Suherli et al. 2026), we also show fit results in Table 6 for a distance of 1 kpc. As expected, the main effect of assuming a smaller distance is a decrease in the emission radius, so that  $R_{\text{em}}/d$  is approximately constant. However, there is also an accompanying small decrease in the temperature  $T_{\text{eff},2}$  of the colder surface.

The right panel of Figure 5 shows that our best-fit magnetic hydrogen atmosphere result has spectral features due to transitions at the harmonics  $n$  of the electron cyclotron resonance (redshifted) at

$$E_B^\infty = (\hbar e B / m_e c) / (1 + z_g) = 115.8 \text{ eV} (B/10^{10} \text{ G}) / (1 + z_g) \quad (1)$$

(see, e.g., Pavlov & Shibakov 1978; Potekhin 2010; Suleimanov et al. 2012; Potekhin et al. 2014). At  $B = 3.16 \times 10^{10}$  G and  $1 + z_g = 1.235$ , the strongest two lines are at 0.59 keV for the  $n = 2$  harmonic and 0.89 keV for the  $n = 3$  harmonic, while the fundamental ( $n = 1$ ) at 0.3 keV is below the energy range we are sensitive to here. Note also that the best-fit for emission by the dominant hot spot component has  $B = 7 \times 10^{11}$  G, such

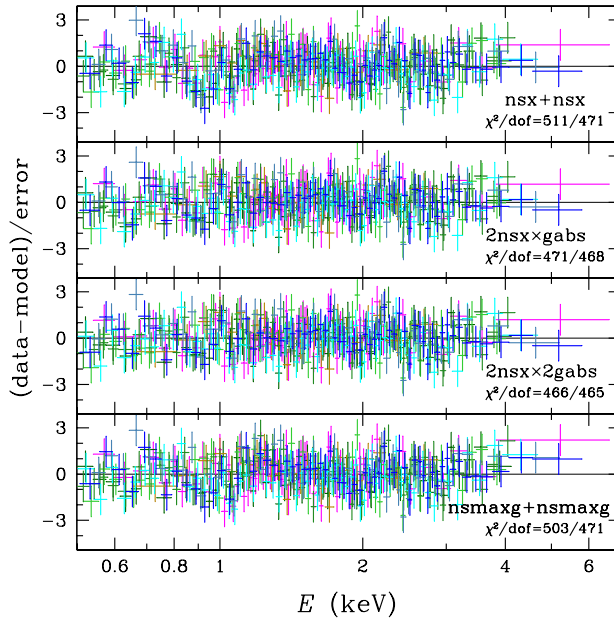


**Figure 6.** Best-fit residuals using spectral models made up of two partially ionized hydrogen atmosphere components. The top panel shows results of non-magnetic nsx+nsx, while the bottom panel shows magnetic nsmaxg+nsmaxg with  $B = 3.16 \times 10^{10}$  G and  $7 \times 10^{11}$  G for the two components (these are the same as in Figure 5). The middle two panels show results using nsx+nsx and including one or two Gaussian absorption lines with gabs.

that  $E_B^\infty = 6.6$  keV is located where the measured flux is low. It is important to point out that (a) we fixed the NS parameters  $M$  and  $R$  such that the redshift factor  $1 + z_g$  is also fixed and (b) the redshift factor is degenerate with magnetic field  $B$  in determining the observed cyclotron energy, such that a 10 percent difference in redshift factor would lead to a 10 percent difference in  $B$ . If we allow the radius to be different from 12 km, we find a slightly better fit ( $\Delta\chi^2 \approx 2$ ) with a larger radius of 13.5 km ( $\pm 1$  km), which corresponds to a redshift factor of 1.20.

We also computed spectral models at  $B = 3.16 \times 10^{10}$  G but with the magnetic field direction  $\Theta_B = \pi/2$ , i.e., tangential to the surface rather than normal to it. We find these spectra lead to a very slightly worse fit ( $\Delta\chi^2 = 1$ ). This is in part because, at the best-fit  $T_{\text{eff}}$ , the harmonics above the fundamental are somewhat weaker and narrower than when the atmosphere models have  $\Theta_B = 0$ . We explore next the strength and broadness of the spectral features.

The predicted resonance features at low energies from the magnetic model at  $B \approx 3 \times 10^{10}$  G contribute to a better overall fit compared to the blackbody and non-magnetic models considered above, in particular by reducing the amplitude of what seems to be systematic oscillatory behaviour in the fit residuals at  $E < 1$  keV seen in Figure 1 and the left panel of Figure 5. These oscillations appear to have minima at  $\sim 0.6$  keV and  $0.9$  keV. To better characterize these observed spectral features independent of the magnetic field, we fit the data using a model composed of nsx+nsx convolved with either one or two Gaussian absorption lines modeled by gabs. The results are given in Tables 6 and 7, and residuals of the best-fits are shown in Figure 6. Most of the best-fit parameters are within the uncertainties of the nsx+nsx model that does not include the Gaussian absorption lines, but the fit is greatly improved by the presence of a line at  $\sim 0.92$  eV and a second line at 0.6 keV. A f-test comparison of the fit

statistics,  $\chi^2/\text{dof} = 471/468$  versus  $511/471$ , gives a probability of  $3 \times 10^{-8}$ , or  $\approx 5\sigma$ , for one line ( $1 \times 10^{-7}$  for two lines); note the f-test probability is 0.17 when comparing results of one versus two lines. Similar levels of fit improvement are obtained when using instead a minimum of 25 or 200 counts per bin.

Since cyclotron absorption lines at a single magnetic field are better described as Lorentzian in shape, rather than Gaussian, we also performed fits using lorabs instead of gabs. These fits are slightly worse  $\Delta\chi^2 < 7$  and require larger line widths. The better fit by non-magnetic models with broader Gaussian-shaped absorption lines may be indicating that the magnetic field across most of the surface varies by a small amount, near that of our magnetic model with  $B = 3.16 \times 10^{10}$  G.

## 4 DISCUSSION

We presented analysis of all the high-quality archival spectra of the CCO in the Vela Junior SNR taken by Chandra and XMM-Newton from 2001 to 2010. Each spectrum is generally well-fit by primarily thermal models, e.g., two blackbodies or a blackbody and power law. The spectral model parameters and flux do not differ significantly and thus are constant between epochs. As a result, we fit all the spectra simultaneously to obtain more robust measurements of the flux and spectral parameters of Vela Junior. We find that more physically-motivated NS atmosphere models can fit the joint spectra, and these include an atmosphere composed of partially ionized hydrogen at low ( $B < 10^9$  G) or moderate ( $B \sim 10^{12}$  G) magnetic field strengths with a small hot spot at  $T_{\text{eff}} \approx 3.5 \times 10^6$  K. The remaining NS surface is at a lower temperature  $T_{\text{eff}} \approx (6.6 - 8.8) \times 10^5$  K (range here spans the range of median  $T_{\text{eff},2}$  given for fits at 1.4 kpc in Table 6, which is larger than their individual uncertainty) and a lower magnetic field. There are indications of absorption features at 0.6 keV and 0.9 keV, which could be due to harmonics of the electron cyclotron resonance at a magnetic field of  $3 \times 10^{10}$  G. Such a magnetic field is similar to the fields seen in three other CCOs. It would be valuable to verify the presence of these absorption features with a much longer observation or more sensitive instrument.

No matter the spectral model, the measured absorbed 0.5–8 keV flux is  $\approx 1.25 \times 10^{-12}$  erg cm $^{-2}$  s $^{-1}$ , and the unabsorbed total flux is  $\approx 2.2 \times 10^{-12}$  erg cm $^{-2}$  s $^{-1}$ . Therefore, at a distance of  $1.4 \pm 0.1$  kpc (Suherli et al. 2026), the bolometric luminosity is  $(5 \pm 1) \times 10^{32}$  erg s $^{-1}$ , which is mainly due to the hot spot. In contrast, the approximate average luminosity from the entire 12 km cool surface is  $L^\infty \approx (1.3 - 4.0) \times 10^{32}$  erg s $^{-1}$ . Note that Marino et al. (2024) derived similar luminosities for their NS cooling study, despite using a smaller distance to Vela Jr. This is because they only used the ACIS-S CC observation, which yields a higher flux due to contamination by the SNR and poorer spectral modelling and fits when only this data is considered (see Section 3 and Table 2, as well as discussions in Becker et al. 2006).

The small hot spot that we find for Vela Junior could lead to X-ray pulsations at the NS spin period like those seen for three CCOs (Zavlin et al. 2000; Gotthelf et al. 2005; Gotthelf & Halpern 2009). However, searches for pulsations using XMM-Newton pn data yielded a pulsed fraction limit of 5 percent (Alford & Halpern 2023; see also Wu et al. 2021). Such non-detections thus far could simply be due to an unfavorable viewing geometry or a hot spot located on the rotation axis.

Finally, we examine here the impact on NS cooling theory of our measurements of flux/luminosity and temperature of Vela Junior. In Figure 7, we plot the luminosity and temperature, assuming an age

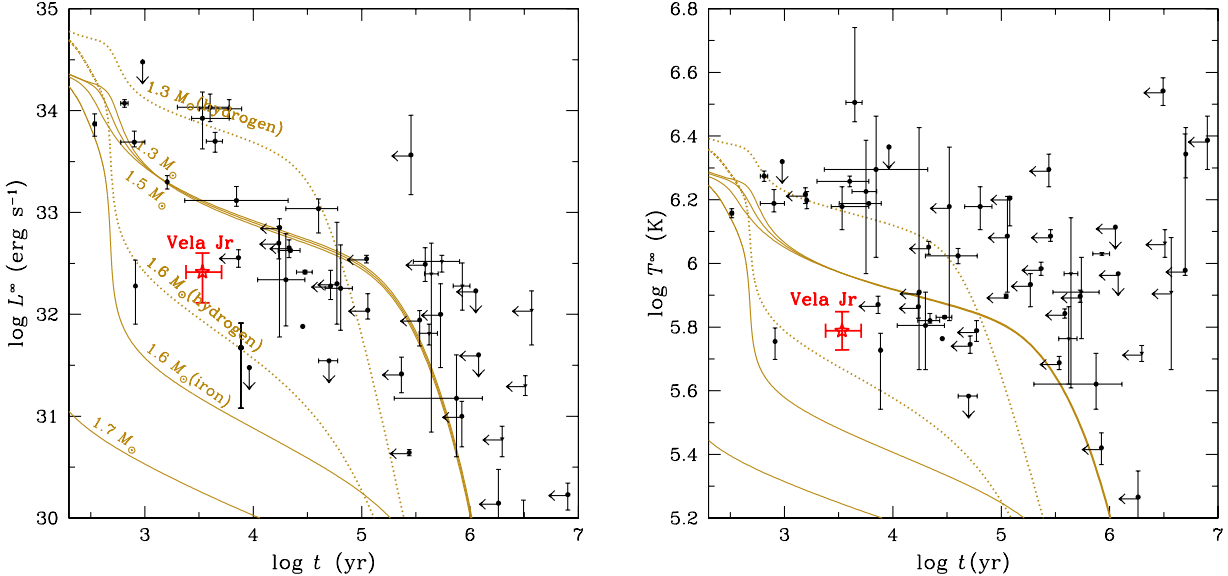


**Figure 7.** Observed luminosity  $L^\infty$  (left) and temperature  $T^\infty$  (right) as functions of NS age. Data points are from Potekhin et al. (2020); Ho et al. (2024) (see also <https://www.ioffe.ru/astro/NSG/thermal/>), except the stars which denote Vela Junior. Solid lines show cooling curves from NS cooling simulations for NS masses  $M = 1.3, 1.4, 1.5, 1.6$ , and  $1.7 M_\odot$  (from top to bottom) using the BSk24 nuclear equation of state and an iron envelope and including neutron superfluidity in the crust and core and proton superconductivity in the core, while dashed lines are for a hydrogen envelope; note that direct Urca cooling becomes active for BSk24 at  $M > 1.59 M_\odot$ . See text for more details.

of 2.4–5.1 kyr (Allen et al. 2015). For the luminosity, we use the average value from the entire surface since the total measured luminosity is dominated by emission from the small hot spot, as shown by Figure 5. Similarly with the temperature, we use the value from the colder component that represents the temperature of most of the cool surface. The ranges in  $L^\infty$  and  $T^\infty$  use the range of median  $T_{\text{eff},2}$  in Table 6, which is larger than the uncertainty in each  $T_{\text{eff},2}$ . Also shown are the luminosity and temperature of other NSs of various ages (Potekhin et al. 2020; Ho et al. 2024). The luminosity, temperature, and age of Vela Junior place it near several other young NSs, in particular, PSR J0205+6449 in the 3C 58 SNR with  $L^\infty \sim 2 \times 10^{32} \text{ erg s}^{-1}$ ,  $\log T^\infty \approx 5.8$ , and age = 845 yr (Slane et al. 2004; Kothes 2013; Potekhin et al. 2020; Marino et al. 2024), PSR B2334+61 in the G114.3+0.3 SNR with  $L^\infty \sim 5 \times 10^{31} \text{ erg s}^{-1}$ ,  $\log T_{\text{eff}} \approx 5.6$ , and age  $\sim 7.7$  kyr (Yar-Uyaniker et al. 2004; McGowan et al. 2006; Potekhin et al. 2020; Marino et al. 2024), and PSR J0007+7303 in the CTA 1 SNR with  $L^\infty < 3 \times 10^{31} \text{ erg s}^{-1}$ ,  $\log T_{\text{eff}} < 6.4$ , and age  $\sim 9$  kyr (Caraveo et al. 2010; Martín et al. 2016; Potekhin et al. 2020). Vela Junior, these three young NSs, and a few others appear much less luminous and cooler than most other NSs of similar ages.

Figure 7 also shows the luminosity and temperature evolutions calculated from NS cooling simulations (see Ho et al. 2024, for details). These simulations use a particular nuclear equation of state, BSk24 (Pearson et al. 2018), and superconducting and superfluid energy gaps. But it is important to note that cooling evolutions can vary greatly depending on which equation of state and energy gaps are used. Nevertheless, the behaviour, especially regarding direct Urca cooling and NS mass, are still qualitatively similar despite differences in theoretical models (see, e.g., reviews by Yakovlev & Pethick 2004; Potekhin et al. 2015). For the BSk24 equation of state, it has a threshold mass of  $1.59 M_\odot$ , above which the proton fraction in the NS core is high enough that fast neutrino emission from direct Urca processes is activated. Meanwhile, some equations of state, such as BSk26 (Pearson et al. 2018) and SLy4 (Douchin & Haensel

2001), do not have a threshold mass below their predicted maximum mass, and thus fast direct Urca cooling never occurs for these equations of state. Below the threshold, NSs cool predominantly by slow neutrino emission from modified Urca processes, which can be enhanced by Cooper pair breaking and formation processes (Gusakov et al. 2004; Page et al. 2004). Thus, we see from Figure 7 that most NSs have a mass lower than a threshold mass. On the other hand, colder NSs point to the existence of cooling by direct Urca processes and hence a nuclear equation of state that allows for such fast cooling. The results we derived here more robustly, by using all available X-ray spectral data and a wide range of spectral models, indicate that, like PSR J0205+6449 (Page et al. 2004; Slane et al. 2004; Yakovlev & Pethick 2004), PSR B2334+61 (Page et al. 2009), and PSR J0007+7303 (Page et al. 2004, 2009), Vela Junior is a strong candidate to be used for this purpose.

## ACKNOWLEDGEMENTS

WCGH thanks Peter Shternin for providing the results of his spectral analysis. The authors thank the anonymous referee for comments that led to improvements in the paper. This research made use of data obtained from the Chandra Data Archive and the Chandra Source Catalog, and software provided by the Chandra X-ray Center (CXC) in the application packages CIAO and Sherpa. This work is based on observations obtained with XMM-Newton, an ESA science mission with instruments and contributions directly funded by ESA Member States and NASA. This work uses data and software provided by the High Energy Astrophysics Science Archive Research Center (HEASARC), which is a service of the Astrophysics Science Division at NASA/GSFC and High Energy Astrophysics Division of the Smithsonian Astrophysical Observatory. This work made extensive use of the NASA Astrophysics Data System (ADS) Bibliographic Services and the arXiv.

## DATA AVAILABILITY

Data underlying this article will be shared on reasonable request to the corresponding author.

## REFERENCES

Acero F., Gallant Y., Ballet J., Renaud M., Terrier R., 2013, *A&A*, **551**, A7

Alford J. A. J., Halpern J. P., 2023, *ApJ*, **944**, 36

Allen G. E., Chow K., DeLaney T., Filipović M. D., Houck J. C., Pannuti T. G., Stage M. D., 2015, *ApJ*, **798**, 82

Arnaud K. A., 1996, in Jacoby G. H., Barnes J., eds, *Astronomical Society of the Pacific Conference Series* Vol. 101, *Astronomical Data Analysis Software and Systems* V. p. 17

Aschenbach B., 1998, *Nature*, **396**, 141

Becker W., Hui C. Y., Aschenbach B., Iyudin A., 2006, *arXiv e-prints*, pp [astro-ph/0607081](#)

Bignami G. F., Caraveo P. A., De Luca A., Mereghetti S., 2003, *Nature*, **423**, 725

Burgio G. F., Schulze H.-J., Vidaña I., Wei J.-B., 2021, *Progress in Particle and Nuclear Physics*, **120**, 103879

Camilli F., Becker W., Predehl P., Dennerl K., Freyberg M., Mayer M. G. F., Sasaki M., 2023, *A&A*, **673**, A45

Caraveo P. A., De Luca A., Marelli M., Bignami G. F., Ray P. S., Saz Parkinson P. M., Kanbach G., 2010, *ApJ*, **725**, L6

Chang P., Bildsten L., Arras P., 2010, *ApJ*, **723**, 719

De Luca A., 2008, in Bassa C., Wang Z., Cumming A., Kaspi V. M., eds, *American Institute of Physics Conference Series* Vol. 983, *40 Years of Pulsars: Millisecond Pulsars, Magnetars and More*. AIP, pp 311–319 ([arXiv:0712.2209](#)), doi:10.1063/1.2900173

De Luca A., 2017, in *Journal of Physics Conference Series*. IOP, p. 012006 ([arXiv:1711.07210](#)), doi:10.1088/1742-6596/932/1/012006

Douchin F., Haensel P., 2001, *A&A*, **380**, 151

Fruscione A., et al., 2006, in Silva D. R., Doxsey R. E., eds, *Society of Photo-Optical Instrumentation Engineers (SPIE) Conference Series* Vol. 6270, *Society of Photo-Optical Instrumentation Engineers (SPIE) Conference Series*. p. 62701V, doi:10.1117/12.671760

Gotthelf E. V., Halpern J. P., 2009, *ApJ*, **695**, L35

Gotthelf E. V., Halpern J. P., Seward F. D., 2005, *ApJ*, **627**, 390

Gotthelf E. V., Halpern J. P., Alford J., 2013, *ApJ*, **765**, 58

Gusakov M. E., Kaminker A. D., Yakovlev D. G., Gnedin O. Y., 2004, *A&A*, **423**, 1063

Halpern J. P., Gotthelf E. V., 2010, *ApJ*, **709**, 436

Ho W. C. G., 2014, in Petit P., Jardine M., Spruit H. C., eds, *IAU Symposium* Vol. 302, *Magnetic Fields throughout Stellar Evolution*. pp 435–438 ([arXiv:1311.5583](#)), doi:10.1017/S1743921314002683

Ho W. C. G., Heinke C. O., 2009, *Nature*, **462**, 71

Ho W. C. G., Potekhin A. Y., Chabrier G., 2008, *ApJS*, **178**, 102

Ho W. C. G., Pol N., Deller A. T., Becker W., Burke-Spolaor S., 2024, *Publ. Astron. Soc. Australia*, **41**, e066

Kargaltsev O., Pavlov G. G., Sanwal D., Garmire G. P., 2002, *ApJ*, **580**, 1060

Kothes R., 2013, *A&A*, **560**, A18

Lattimer J. M., Pethick C. J., Prakash M., Haensel P., 1991, *Phys. Rev. Lett.*, **66**, 2701

Marino A., Dehman C., Kovlakas K., Rea N., Pons J. A., Viganò D., 2024, *Nature Astronomy*, **8**, 1020

Martín J., Torres D. F., Pedaletti G., 2016, *MNRAS*, **459**, 3868

McGowan K. E., Zane S., Cropper M., Vestrand W. T., Ho C., 2006, *ApJ*, **639**, 377

Mereghetti S., De Luca A., Caraveo P. A., Becker W., Mignani R., Bignami G. F., 2002, *ApJ*, **581**, 1280

Mignani R. P., De Luca A., Zharikov S., Hummel W., Becker W., Pellizzoni A., 2019, *MNRAS*, **486**, 5716

Mori K., Ho W. C. G., 2007, *MNRAS*, **377**, 905

Page D., Applegate J. H., 1992, *ApJ*, **394**, L17

Page D., Lattimer J. M., Prakash M., Steiner A. W., 2004, *ApJS*, **155**, 623

Page D., Lattimer J. M., Prakash M., Steiner A. W., 2009, *ApJ*, **707**, 1131

Page D., Prakash M., Lattimer J. M., Steiner A. W., 2011, *Phys. Rev. Lett.*, **106**, 081101

Pavlov G. G., Shibanov I. A., 1978, *Soviet Ast.*, **22**, 214

Pavlov G. G., Sanwal D., Kızıltan B., Garmire G. P., 2001, *ApJ*, **559**, L131

Pearson J. M., Chamel N., Potekhin A. Y., Fantina A. F., Ducoin C., Dutta A. K., Goriely S., 2018, *MNRAS*, **481**, 2994

Potekhin A. Y., 2010, *A&A*, **518**, A24

Potekhin A. Y., Yakovlev D. G., 2026, *Journal of High Energy Astrophysics*, **49**, 100441

Potekhin A. Y., Chabrier G., Ho W. C. G., 2014, *A&A*, **572**, A69

Potekhin A. Y., Pons J. A., Page D., 2015, *Space Sci. Rev.*, **191**, 239

Potekhin A. Y., Zyuzin D. A., Yakovlev D. G., Beznogov M. V., Shibanov Y. A., 2020, *MNRAS*, **496**, 5052

Sanwal D., Pavlov G. G., Zavlin V. E., Teter M. A., 2002, *ApJ*, **574**, L61

Shternin P. S., Yakovlev D. G., Heinke C. O., Ho W. C. G., Patnaude D. J., 2011, *MNRAS*, **412**, L108

Shternin P. S., Ofengeim D. D., Heinke C. O., Ho W. C. G., 2023, *MNRAS*, **518**, 2775

Slane P., Hughes J. P., Edgar R. J., Plucinsky P. P., Miyata E., Tsunemi H., Aschenbach B., 2001, *ApJ*, **548**, 814

Slane P., Helfand D. J., van der Swaluw E., Murray S. S., 2004, *ApJ*, **616**, 403

Suherli J., et al., 2026, *ApJ*, in press

Suleimanov V. F., Pavlov G. G., Werner K., 2012, *ApJ*, **751**, 15

Verner D. A., Ferland G. J., Korista K. T., Yakovlev D. G., 1996, *ApJ*, **465**, 487

Wijngaarden M. J. P., Ho W. C. G., Chang P., Heinke C. O., Page D., Beznogov M., Patnaude D. J., 2019, *MNRAS*, **484**, 974

Wilms J., Allen A., McCray R., 2000, *ApJ*, **542**, 914

Wu Q., Pires A. M., Schworer A., Xiao G.-C., Yan S.-P., Ji L., 2021, *Research in Astronomy and Astrophysics*, **21**, 294

Yakovlev D. G., Pethick C. J., 2004, *ARA&A*, **42**, 169

Yar-Uyaniker A., Uyaniker B., Kothes R., 2004, *ApJ*, **616**, 247

Zavlin V. E., Pavlov G. G., Sanwal D., Trümper J., 2000, *ApJ*, **540**, L25

Zhao J., Heinke C. O., Shternin P. S., Ho W. C. G., Ofengeim D. D., Patnaude D., 2025, *ApJ*, **991**, 136

This paper has been typeset from a  $\text{\TeX}$ / $\text{\LaTeX}$  file prepared by the author.